5.1 Irradiation Response of Next Generation High Temperature Superconducting Rare-earth and Nanoparticle-Doped $YBa_2Cu_3O_{7-x}$ Coated Conductors for Fusion Energy Applications — K.J. Leonard, T. Aytug (Oak Ridge National Laboratory), A. Perez-Bergquist, W.J. Weber (University of Tennessee), and A. Gapud (University of South Alabama)

OBJECTIVE

The goal of this work is to evaluate the irradiation response of the newest generation of coated conductors based on rare earth and nanoparticle doping of the $YBa_2Cu_3O_{7-x}$ (YBCO) high temperature superconductor. The materials under investigation represent different methods for enhanced flux pinning for improved performance under externally applied magnetic fields. Ion beam irradiation will be used to simulate neutron damage cascades in the materials to examine the effect that radiation damage has on the different pre-existing defect structures used for flux pinning and to assess the superconductors capability for use in fusion reactor systems.

SUMMARY

The pre-irradiation electrical and microstructural characterization of three advanced high temperature superconductors has been completed and is discussed in this report. These conductors represent three distinct ways in which increased performance and improved flux pinning have been achieved through means of rare earth and nanoparticle doping. The $GdBa_2Cu_3O_{7-x}$ conductor primarily utilizes stacking fault and anti-domain defects in its structure to enhance magnetic flux pinning in the B//ab direction. Disperse $(Dy,Y)_2O_3$ nano-particles dominate the microstructure of the $(Y,Dy)Ba_2Cu_3O_{7-x}$ conductor which also shows enhanced B//ab pinning. The Zr-doping of $YBa_2Cu_3O_{7-x}$ produces c-axis aligned $BaZrO_3$ nanoparticles to produce enhanced B//c pinning and a reduced field dependence of the critical current density. Irradiation experiments using 25 MeV Au ions will begin at the start 2013, from which the response behavior of these advanced conductors will be evaluated.

PROGRESS AND STATUS

Introduction

In an effort to reduce reactor complexity and costs, the ORNL Fusion Materials Program is evaluating the irradiation response of the newest generation of $YBa_2Cu_3O_{7-x}$ (YBCO) high temperature superconducting (HTS) materials for possible qualification in future magnetic confinement reactor designs. In addition to the higher critical temperature over currently used Nb_3Sn (T_c = 92 K versus 18 K for Nb_3Sn), YBCO conductors offer higher critical current density (J_c) values, a smaller flux pinning coherency length that can produce J_c increases on exposure to neutron irradiation up to $1x10^{22}$ n/m^2 (E>0.1 MeV) [1-10] and a smaller effective neutron capture cross section. However, in the past, HTS materials have been limited to self-field applications such as power transmission cables due to their inability to maintain magnetic flux pinning under externally applied fields [10-11]. The newest generation of YBCO conductors incorporate the use of engineered textured substrates and nanoparticle additions to the conductor to produce correlated defect structures in the YBCO lattice that increase J_c values with reduced dependence on magnetic field [13-18].

The first stage of this work is to examine the room temperature ion-irradiated properties of the latest generation of rare earth and nanoparticle doped YBCO coated conductors for their potential use in nuclear environments. Providing a first investigation into both the radiation-induced generation of defects and the changes to pre-existing pinning centers for these materials. Establishing a fundamental understanding of the irradiation properties of these nano-doped materials may lead to further development of new ceramic materials used in diagnostic systems for ITER, DEMO and eventual fusion power plants.

Materials

The materials include $(Y,Dy)Ba_2Cu_3O_{7-x}$ supplied by American Superconductor (AMSC), $Gd_2Ba_2Cu_3O_{7-x}$ and Zr-doped $(Y,Gd)Ba_2Cu_3O_{7-x}$ purchased from SuperPower (SP). At this time, Nb-doped YBCO material has not been fabricated due to budgetary considerations, as this material will require in-house fabrication. The $GdBa_2Cu_3O_{7-x}$ (GBCO) tapes will represent a condition in which nanoparticles are not introduced into the standard $YBa_2Cu_3O_{7-x}$ conductor. The substitution of Gd for Y in the 123 structure offers a high performance conductor, which is in-line with the general goals of this research in examining high performance production quality tapes. Furthermore, cables made of GBCO based conductors demonstrate less critical current dependence, or degradation, to cable straining than YBCO based conductors for the same buffer/substrate architecture as used in this study [19,20]. A list of the materials of interest to this study and the general features of the HTS layer are provided in Table 1. The buffer architecture for the AMSC and SP produced tapes is illustrated in Figure 1. The high temperature superconducting (HTS) layers are produced through metalorganic chemical vapor deposition (MOCVD) onto the buffered Ni-alloy tapes. The biaxial texturing of the YBCO needed for superconducting current flow along the length of tape is generated from either the rolling assisted bi-axial texturing of the metallic substrate, AMSC architecture, or developed within the buffer layer as in the case of the SP materials.

Table 1. List of the high temperature superconductors, substrate architecture (listed by company name from which tapes were fabricated) and the type of flux pinning created for improved use in magnetic field applications.

Material	Substrate	Features
$(Y,Dy)Ba_2Cu_3O_{7-x}$	American Superconductor	50% substitution of Y in $YBa_2Cu_3O_{7-x}$ chemistry. Development of $(Dy,Y)_2O_3$ nanoparticles, enhanced H//ab pinning. Increased stacking faults ($YBa_2Cu_4O_8$ intergrowths) in the film.
$GdBa_2Cu_3O_{7-x}$	SuperPower	Substitution of Gd for Y in the $YBa_2Cu_3O_{7-x}$ chemistry. High density stacking fault generation from mismatch in growth domains from buffer and Gd_2O_3 particles, yielding improvements in H//ab pinning.
Zr-doped $(Y,Gd)Ba_2Cu_3O_{7-x}$	SuperPower	Creation of $BaZrO_3$ nanodots aligned along the c-axis direction, producing enhanced H//c pinning.
Nb-doped $YBa_2Cu_3O_{7-x}$	SuperPower	YBa_2NbO_6 nanoparticle alignment in c-axis direction, for enhanced H//c pinning, in addition to increased H//ab pinning from stacking faults generated.

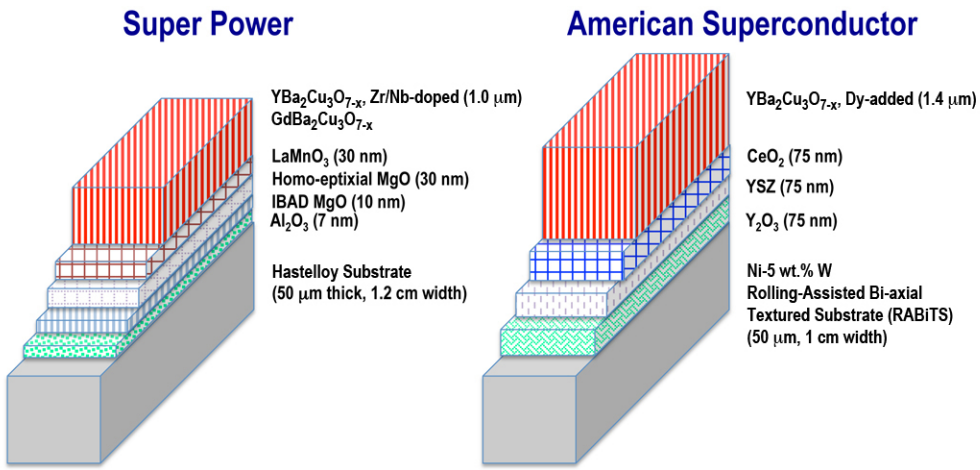

Figure 1. Schematic of the two buffer layer architectures used in this work.

Experimental Procedure

The as purchased long-length Zr-doped $(Y,Gd)Ba_2Cu_3O_{7-x}$ and $(Y,Dy)Ba_2Cu_3O_{7-x}$ conductors showed critical current, I_c, values in self-field of approximately 239 A/cm-width and 525 A/cm-width, respectively, across the 1 meter length tapes received. These tapes have been cut down into smaller test samples and for the case of the Zr-YBCO material, the Ag overlay coating was removed through etching. The purchased $Gd_2Ba_2Cu_3O_{7-x}$ samples were already pre-cut into smaller test specimens. Patterned current bridges were laser scribed into the HTS test samples for electrical characterization tests in order to accommodate on the available measurement equipment these high current-carrying tapes. Silver was deposited at specific sites for the pad positions of the four-probe voltage and current contacts. Following this, the samples were given a thermal anneal in oxygen at 500°C for 1 hour.

Field dependence characterizations of J_c as a function of applied magnetic field strength, and resistance versus temperature measurements were performed at the University of South Alabama. Angular dependence of I_c with field measurements was performed at ORNL. Pre-irradiation characterization of the specific test samples will allow for the precise assessment of each samples response to irradiation without the influence of possible variations occurring along the full-length tapes.

Transmission electron microscopy (TEM) characterization was performed using a Philips/FEI CM200 instrument at ORNL. Samples for TEM analysis were created through focus ion beam (FIB) milling the HTS samples using a FEI Quanta 3D 200i dual beam instrument. Care was taken in minimizing ion beam created damage during processing, with final thinning of the specimen performed down to a 2 kV,8.9 pA, beam conditions using the Ga ion source.

Ion irradiation will be performed at low energy levels typical of simulating cascade damage to avoid columnar defect formation that occurs when the electronic energy loss of the irradiating ions is above 20 keV/nm [21-23]. Computational analysis of energy loss profiles through the HTS tapes was performed using TRIM calculations to evaluate the electronic energy loss, penetration depths and collision events for 10 MeV O, 25 MeV Cu, and 25 MeV Au irradiations. To achieve a significant number of collisions occurring in the 1-1.4 mm thick HTS layer, 25 MeV

Au ion irradiations were selected for this testing. Based on TRIM calculations and estimates from published data [22,24], fluence ranges to be examined for the 25 MeV Au irradiations will be between 10^{10} and 10^{13} ions/cm^2. The first round of Ion irradiation of the HTS conductors will be completed in the first week in January of 2013, at a fluence of 10^{12} ions/cm^2. The fluence selected will be high enough to provide an initial feedback to our estimates, without exceeding conditions where J_c values fall due to excessive damage to the HTS structure.

RESULTS

Pre-irradiation characterization of the superconducting properties and microstructure has been completed for the material obtained to date. The microstructure of the $(Y,Dy)Ba_2Cu_3O_{7-x}$ conductor (Figure 2) is characterized by spherical shaped $(Y,Dy)_2O_3$ particles in the 123 matrix. Energy dispersive X-ray spectroscopy (EDS) analysis determined that Dy is substituting approximately 43% for Y in the 123 matrix and 39.2% for Y in the $(Y,Dy)_2O_3$ nanoparticles. The average $(Y,Dy)_2O_3$ particle size and density are measured at 26 nm and 4.7×10^{21} m^{-3}, respectively. These particles are cubic structured and do not display any specific orientation relationship to the 123 matrix. However, examples are found that show shapes with sides flattened parallel to the (001) planes of the matrix. Present in the 123 matrix are stacking fault defects identified as intergrowths of $(Y,Dy)Ba_2Cu_4O_8$, assuming that Dy is also substituting for Y in these layers. This 124 structure is similar to the 123 structure, but with the addition of a double Cu-O chain (Y-123, has a single Cu-O chain) that creates the longer c-axis lattice constant of 2.723 nm, versus 1.174 nm for Y-123.

The electrical properties of the pre-irradiated $(Y,Dy)Ba_2Cu_3O_{7-x}$ conductor samples were tested at field strengths up to 1.5 Tesla under varying applied angular field directions (f). The results for one of the test specimens is shown in Figure 3, and reveals that there is no enhanced J_c performance in the condition where the applied magnetic field is parallel to the c-axis (B//c, f=90°). This corroborates with microstructural studies that show only planar defects along the ab-planes are observed. The $(Dy,Y)_2O_3$ particles offer improved properties over that of undoped YBCO over a range of applied field directions, but the lack of particle alignment provides no additional benefit to the conductor properties in the B//c field orientation as compared to that of the B//ab.

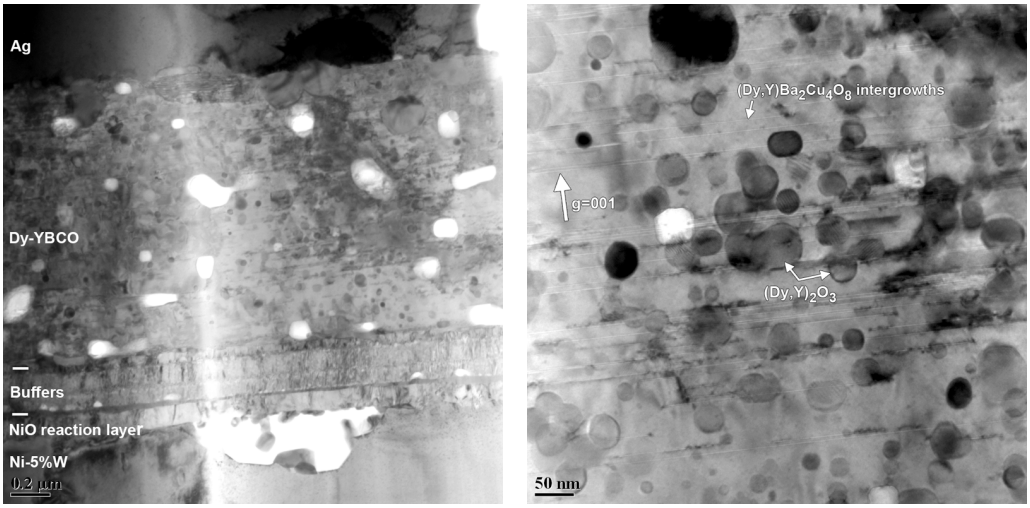

(a) (b)

Figure 2. Transmission electron micrographs of the $(Y,Dy)Ba_2Cu_3O_{7-x}$ material in the as received, pre-irradiated, condition. (a) Low magnification image showing superconducting layer, buffers and bi-axially textured Ni-5%W substrate. (b) Two-beam image, g=001, of the conductor showing the presence of $(Y,Dy)_2O_3$ particles and $(Y,Dy)Ba_2Cu_4O_8$ intergrowths. The Ag layer on the top of the superconducting film was deposited for the current contact pad used in electrical testing.

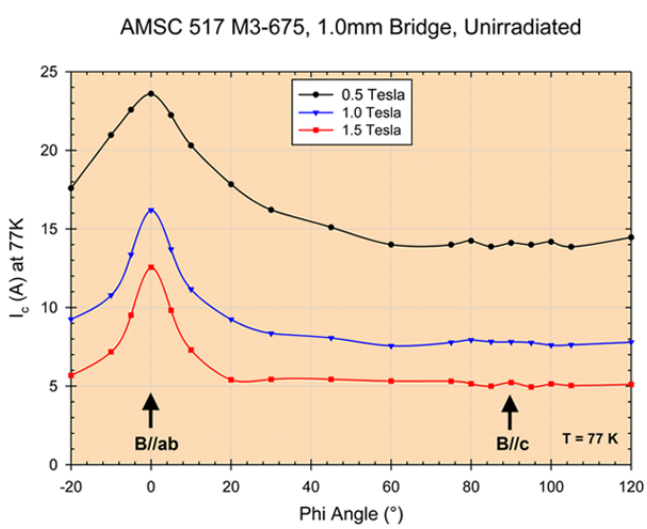

Figure 3. Pre-irradiation critical current versus applied angular field as a function of field strength for $(Y,Dy)Ba_2Cu_3O_{7-x}$, sample AMSC 517, using a 1 mm bridge.

The $GdBa_2Cu_3O_{7-x}$ conductor has a different defect structure than the $(Y,Dy)Ba_2Cu_3O_{7-x}$ conductor. The 123 growth domains create slight mismatches (less than one unit cell) between each other resulting in a threading defect or anti-phase domain running in the c-axis (tape normal) direction (Figure 4a). The high density of $(Y,Dy)_2O_3$ particles in the $(Y,Dy)Ba_2Cu_3O_{7-x}$ conductor remove these anti-phase domains. The anti-phase domain sites can provide some measure of H//c pinning, but are mainly a source for intergrowths into the 123 structures. These intergrowths, a type of stacking fault, are identified as Gd_2BaCuO_4, which are different than those observed in the $(Y,Dy)Ba_2Cu_3O_{7-x}$ conductor. In both cases the intergrowths provide additional H//ab pinning. The amount of intergrowths is greater in the $GdBa_2Cu_3O_{7-x}$ film than the other conductor types examined, as was evident in the observed streaking in the <001> between the diffracted intensities of the [100] zone axis pattern (not shown). The $GdBa_2Cu_3O_{7-x}$ conductor also contains Gd_2O_3 particles (Figure 4b) with an average size of 3.8 nm and density of $1x10^{22}$ m^{-3}. The Gd_2O_3 particles show an occasional disruption in the 123 stacking sequence resulting in faulted structures being generated. The length of the 211 faults created by the Gd_2O_3 particles is on the order of 10 to 20 nm while those originating at the domain boundaries well exceed these values.

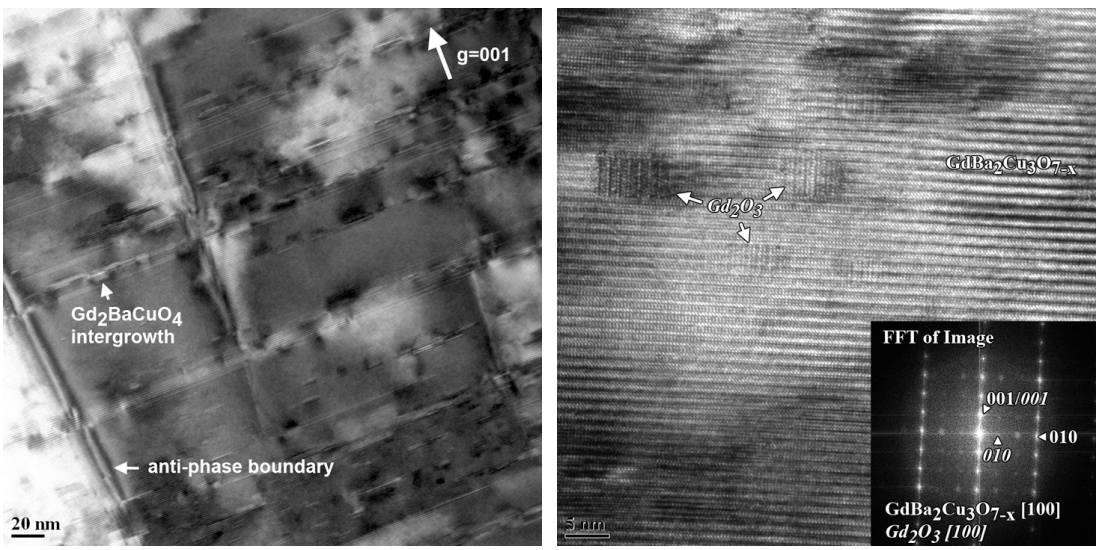

(a) (b)

Figure 4. Transmission electron micrographs of the $GdBa_2Cu_3O_{7-x}$ material in the as-received, pre-irradiated condition. (a) Two beam, g=001, image illustrating the defect structures created in the superconductor resulting in threading anti-phase defect boundaries between different growth domains of the conductor emanating from the buffer interface and Gd_2BaCuO_4 type intergrowths generated from them. (b) High resolution image on the $GdBa_2Cu_3O_{7-x}$[100] zone axis, showing the presence and orientation of Gd_2O_3 particles in the conductor.

The angular field dependence measurement for the pre-irradiated electrical properties of a $GdBa_2Cu_3O_{7-x}$ sample are shown in Figure 5, and similar to that of the $(Y,Dy)Ba_2Cu_3O_{7-x}$ conductor, reveal no enhanced J_c performance in the condition in the B//c condition. This is also not unexpected due to the dominance of the Gd_2BaCuO_4 intergrowths present in the microstructure. While the Gd_2O_3 particles show a strong orientation relationship to the 123 matrix, they are un-oriented in spatial distribution in the conductor. However, the role of the Gd_2O_3 particles appear to increase the amount of intergrowths and may be responsible for the stronger pinning forces appearing in the B//ab condition compared to the $(Y,Dy)Ba_2Cu_3O_{7-x}$ conductor. The positioning of the B//ab peak to f<0° is due to a slight tilt in the orientation of the $(Y,Dy)Ba_2Cu_3O_{7-x}$ conductor relative to the normal of the tape, and is observed in all conductors in this study that were deposited on the SP substrates.

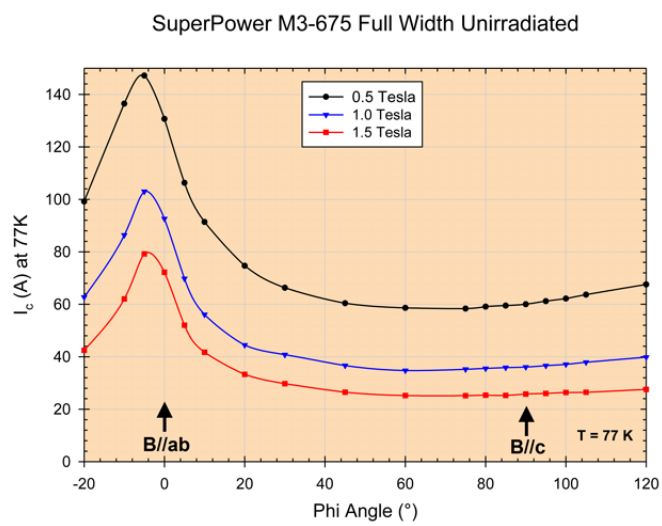

Figure 5. Pre-irradiation critical current versus applied angular field as a function of field strength for $GdBa_2Cu_3O_{7-x}$, sample SPM3-675, full width un-bridged.

The Zr-doping of the $(Y,Gd)Ba_2Cu_3O_{7-x}$ conductor results in a microstructure of $BaZrO_3$ (BZO) particles in the 123 matrix (Figure 6). However, it is apparent that an orientation of the BZO particles deviates at approximately 225 nm above the buffer, from particle alignments along the [100] direction in the 123 matrix to that of the [001]. The cause for this may be related to strain relief during the growth of the film during fabrication, or a change in elemental concentration occurring in the deposition process. Preliminary tilting experiments suggest that there may be a change in orientation relationship between the BZO and 123 structures at the two different levels, but this requires further confirmation through additional high-resolution imaging. The alignment of the BZO particles in the upper portion of the conductor creates a columnar defect structure in the [001] direction that is clearly evident in the g=001 two-beam image. Occasional stacking faults producing an intergrowth of the Y211 type structure are observed, as was also seen in the $GdBa_2Cu_3O_{7-x}$ film. High-resolution images were taken of the BZO particles from the lower (Figure 6c) and upper (Figure 6d) regions of the film. Unfortunately, the TEM foil was thicker than the size of the typical particles and therefore a clear lattice image of the BZO particles could not be easily obtained. One particle near the lower portion of the conducting film was thick enough to perform analysis on, and shows the particle displaying a $[010]_{YBCO}$//

$[100]_{BZO}$, $(001)_{YBCO}//(100)_{BZO}$ orientation relationship. For smaller particle sizes, as those observed in the upper portion of the film, a Moiré fringe pattern is imaged due to the overlapping of the matrix and BZO lattice images.

The amount of Gd substitution in the matrix is approximately 55% based on EDS analysis. While the size of the BZO particles made it difficult to eliminate contributions from the matrix in EDS measurements. A comparison of the ratio between the Gd_M and Cu_K characteristic X-ray intensities was made between spectra taken from BZO and matrix locations. If Gd does not substitute for Zr in the BZO structure, then the Gd_M/Cu_K ratio will remain the same as that of the matrix. However, a 20% average increase in the Gd_M/Cu_{Ka} ratio was observed for the BZO spectra over that of the 123 matrixes, suggesting the presence of Gd in the BZO structure. Further thinning of the TEM foil is required to confirm this data and to perform more conclusive high-resolution imaging of the BZO particles.

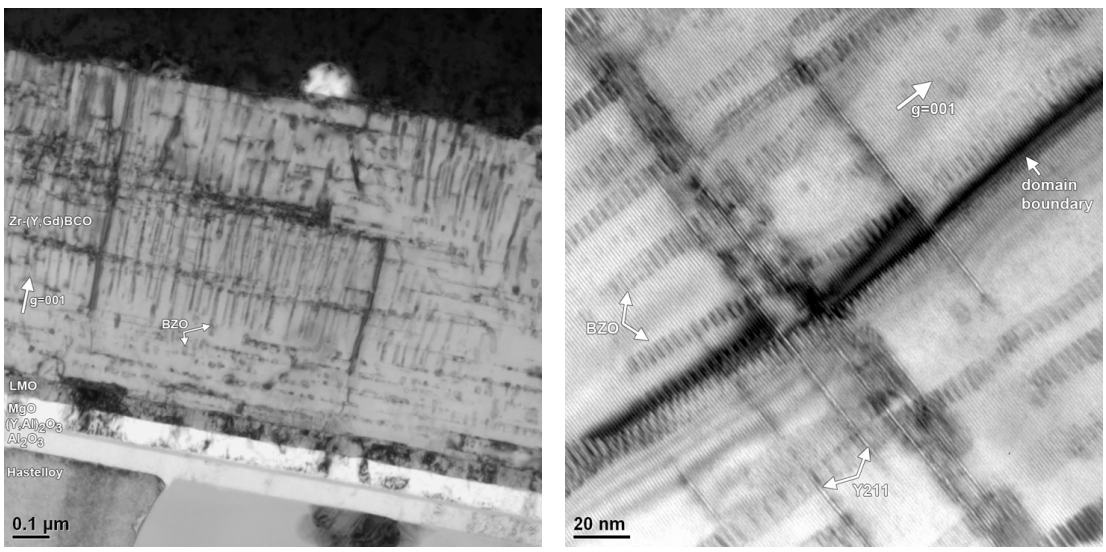

(a) (b)

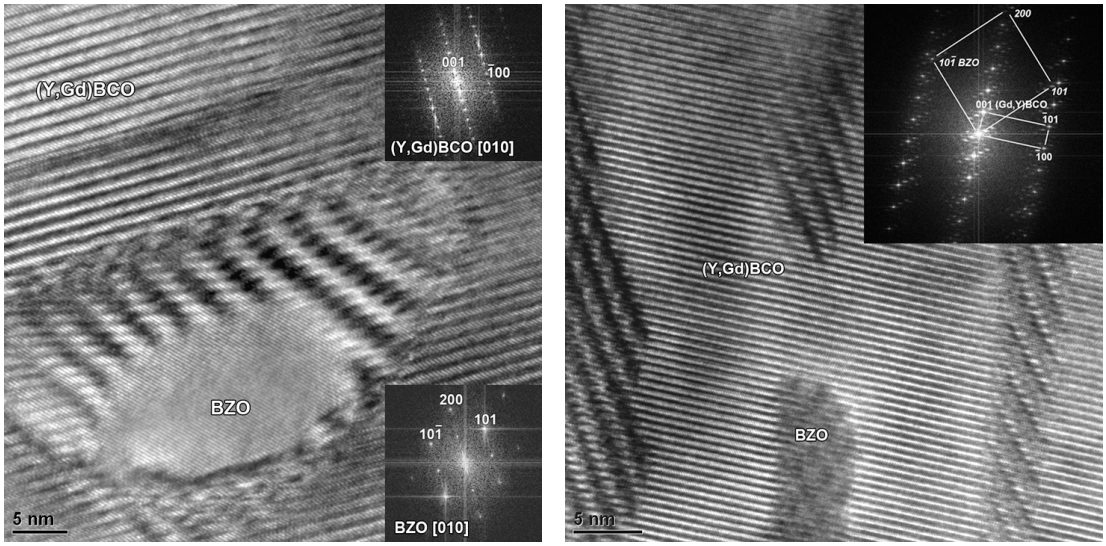

(c) (d)

Figure 6. Transmission electron micrographs of the Zr-doped (Y,Gd)$Ba_2Cu_3O_{7-x}$ material in the as-received, pre-irradiated, condition. (a) Two-beam, g=001 image, illustrating domain boundaries and $BaZrO_3$ (BZO) particle distribution in the superconducting film layer. (b) Higher magnification image under the g=001 condition showing a domain boundary with BZO particles aligned in the c-axis direction. Stacking faults in the conductor are identified as $(Y,Gd)_2BaCuO_4$ (Y211) type. High-resolution images, B=$[010]_{YBCO}$, of the BZO particles (d) near the buffer and (e) at the top of the film. The TEM foil is thicker than most particles, resulting in the Moiré fringe pattern where particles are located.

Due to the alignment of the BZO particles along the c-axis direction (normal to the tape surface), the Zr-doped (Y,Gd)$Ba_2Cu_3O_{7-x}$ material showed a strong increase in pinning in the B//c direction. A comparison of the angular field dependency of the three HTS materials investigated is shown in Figure 7a. The effect of the BZO particles provides near equal I_c measurement in the B//c direction as measured in the B//ab condition dominated by the Y211 intergrowths. It should be cautioned that while the angular field dependency curves for the three HTS materials illustrate the effect of the nanoparticle alignments, comparison between the three samples is not possible due to differences in batches and measurement conditions. However, it is clear that the field dependence of the HTS materials is reduced by the effect of the aligned BZO particles (Figure 7b).

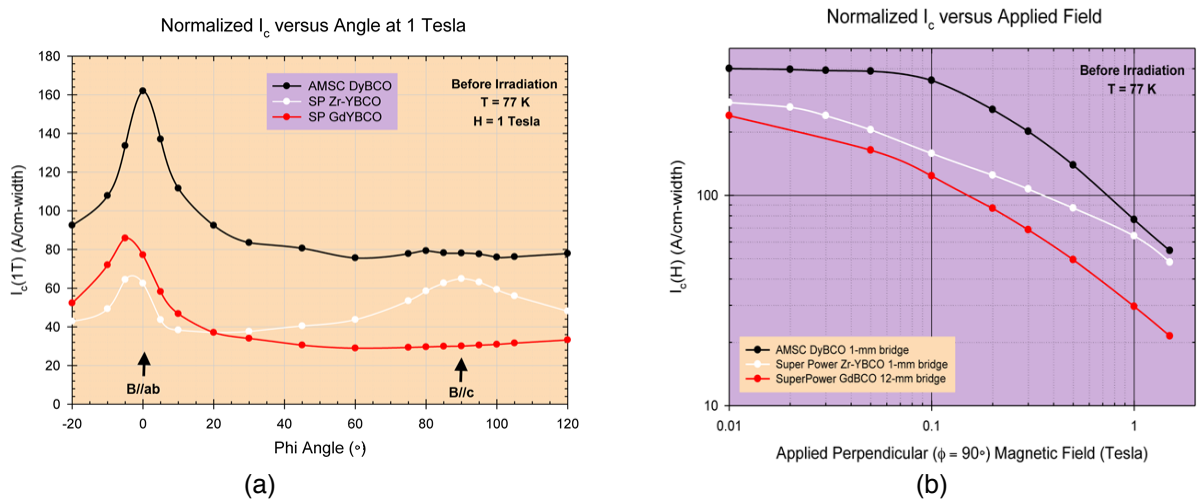

Figure 7. (a) Comparison of the pre-irradiation critical current versus applied angular field as a function of field strength for the $(Y,Dy)Ba_2Cu_3O_{7-x}$, $GdBa_2Cu_3O_{7-x}$, and Zr-doped $(Y,Gd)Ba_2Cu_3O_{7-x}$ samples. (b) Normalized Ic values versus applied field measured under the B//c condition for the various HTS materials examined. Due to difference in sample batches, direct comparisons between sample types is not possible, but general trends in behavior can be observed.

FUTURE WORK

The first round of ion irradiation exposure, 25 MeV Au at 10^{12} ions/cm^2, and post-irradiation testing will begin shortly. Care was taken in measuring the pre-irradiation electrical properties of each HTS sample in order to asses the effects of irradiation damage on their properties and to avoid any variations that may appear in sample to sample batches. This work will provide a first investigation into the radiation effects on the most advanced HTS materials. The effects on superconducting properties through the changes to pre-existing flux pinning centers and the development of radiation-induced defects will be examined through both electrical and microstructural characterization. This work will expand later into low temperature irradiation testing of specific materials that will include *in situ* measurement of self-field superconducting properties as a function of dose, with a further analysis into defect annihilation and the effects of temperature excursions on conductor properties.

REFERENCE

1. H. W. Weber, *Physica C* **185-189** (1991) 309.
2. P. X. Zhang, et al., *Physica C* **282-287** (1997) 1607.
3. F. Vasiliu, V. Sandu, P. Nita, S. Popa, E. Cimpoiasu, and M. C. Bunescu, *Physica C* **303** (1998) 209.
4. D. V. Kulikov, Y. V. Trushin, F. M. Sauerzopf, M. Zehetmayer and H. W. Weber, *Physica C* **355** (2001) 245.
5. U. Topal, H. Sozeri, and H. Yavuz, *Physica C* **408-410** (2004) 636.
6. U. Topal, L. Dorosinskii and H. Sozeri, Physica C **407** (2004) 49.
7. S. Shojaei, R. Khoda-Bakhsh and H. Sedgi, and *J. Supercond. Nov. Magn*. **24** (2008) 387.
8. R. Fuger, M. Esterer, and H. W. Weber, *IEEE Trans. Appl. Supercond.* **19**, 3 (2009) 1532.

9. M. Chudy, R. Fuger, M. Eisterer and H. W. Weber, *IEEE Trans. Appl. Supercond*. **21**, 3 (2011) 3162.
10. T. Nishimura, S. Takeuchi, G. Nishijima, T. Shikama, K. Ochiai, and N. Koizumi, *Fusion Eng. Design* **84** (2009) 1425.
11. D. Larbalestier, A. Gurevich, D. M. Feldmann and A. Polyanski, *Nature* **414** (2001) 368.
12. R. M. Scanlan, A. P. Malozemoff and D. C. Larbalestier, *Proc. IEEE* **92**, 10 (2004) 1639.
13. A. Goyal, et al., *Supercond. Sci. Technol.* **18** (2005) 1533.
14. B. Maiorov, et al., *Nature Mater.* **8**, 5 (2009) 398.
15. S. H. Wee, et al., *Supercond. Sci. Technol*. **21**, 9 (2008) 92001.
16. P. Paturi, et al., *J. Appl. Phys*. **103**, 12 (2008) 123907.
17. S. Kang, et al., *Physica C* **457**, 1-2 (2007) 41.
18. K. Gutierrez, et al., *Nature Mater*. **6**, 5 (2007) 367.
19. D. C. van der Laan, X. F. Lu and L. F. Goodrich, *Supercond. Sci. Technol.* **24** (2011) 042001.
20. D. C. van der Laan, *Supercond. Sci. Technol*. **22** (2009) 065013.
21. N. M. Stickland, N. J. Long, J. Xia, J. Kennedy, A. Markwitz, A. Zondervan, M. W. Rupich, W. Zhang, X. Li, T. Kodenkandath and Y. Huang, *IEEE Trans. Appl. Supercond.* **17**, 2 (2007) 3306.
22. B. Hensel, B. Roas, S. Henke, R. Hopfengärtner, M. Lippert, J. P. Ströbel, M. Vildić and G. Saemann-Ischenko, *Phys. Rev. B* **42**, 7 (1990) 4135.
23. R. Wheeler, M. A. Kirk, A. D. Marwick, L. Civale, and F. H. Holtzberg, *Appl. Phys. Lett*. **63**, 11 (1993) 1573.
24. J. R. Liu, J. Kulik, Y. J. Zhao and W. K. Chu, *Nucl. Instr. Meth. Phys. Res. B* ***80-81*** (1993) 1255.